

## Energy-Efficient Hydrogen Evolution by Fe–S Electrocatalysts: Mechanistic Investigations

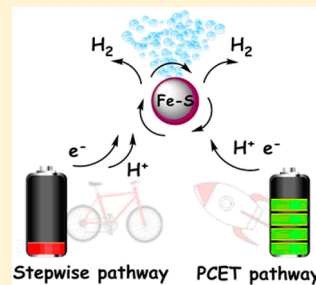
Kai-Ti Chu,<sup>†</sup> Yu-Chiao Liu,<sup>\*,†</sup> Min-Wen Chung,<sup>†</sup> Agus Riyanto Poerwoprajitno,<sup>†</sup> Gene-Hsiang Lee,<sup>‡</sup> and Ming-Hsi Chiang<sup>\*,†</sup>

<sup>†</sup>Institute of Chemistry, Academia Sinica, Nankang, Taipei 115, Taiwan

<sup>‡</sup>Instrumentation Center, National Taiwan University, Taipei 106, Taiwan

### Supporting Information

**ABSTRACT:** The intrinsic catalytic property of a Fe–S complex toward H<sub>2</sub> evolution was investigated in a wide range of acids. The title complex exhibited catalytic events at  $-1.16$  and  $-1.57$  V (vs Fc<sup>+</sup>/Fc) in the presence of trifluoromethanesulfonic acid (HOTf) and trifluoroacetic acid (TFA), respectively. The processes corresponded to the single reduction of the Fe-hydride-S-proton and Fe-hydride species, respectively. When anilinium acid was used, the catalysis occurred at  $-1.16$  V, identical with the working potential of the HOTf catalysis, although the employment of anilinium acid was only capable of achieving the Fe-hydride state on the basis of the spectral and calculated results. The thermodynamics and kinetics of individual steps of the catalysis were analyzed by density functional theory (DFT) calculations and electroanalytical simulations. The stepwise CCE or CE (C, chemical; E, electrochemical) mechanism was operative from the HOTf or TFA source, respectively. In contrast, the involvement of anilinium acid most likely initiated a proton-coupled electron transfer (PCET) pathway that avoided the disfavored intermediate after the initial protonation. Via the PCET pathway, the heterogeneous electron transfer rate was increased and the overpotential was decreased by 0.4 V in comparison with the stepwise pathways. The results showed that the PCET-involved catalysis exhibited substantial kinetic and thermodynamic advantages in comparison to the stepwise pathway; thus, an efficient catalytic system for proton reduction was established.



### INTRODUCTION

The discovery of new types of inexpensive energy resources is important for the global economy, even though recent advances in shale gas extraction technology may provide a temporary solution to the energy shortage in the near future. To address this issue and avoid the tremendous environmental impact from accumulation of greenhouse gases after burnout of fossil fuels, molecular hydrogen is considered as the next-generation fuel.<sup>1,2</sup> Its stored energy (142 MJ/kg) is released accompanied by water formation, which makes H<sub>2</sub> an emission-free energy vector. Industrial production of hydrogen (>75%) currently comes from steam re-forming of hydrocarbons.<sup>3,4</sup> This process requires the use of fossil fuels, mainly natural gas, as a feedstock and elevated working temperatures in the presence of heterogeneous metal catalysts. This is a well-developed and, however, heavily energy consuming process that is accompanied by the generation of CO<sub>2</sub> waste. Electrocatalysis is a promising technology that converts electric energy into chemical bonds. Several metal complexes containing earth-abundant metals such as Fe,<sup>5–15</sup> Ni,<sup>16–22</sup> Co,<sup>23–29</sup> and Mo<sup>30,31</sup> have been examined for potential applications in electrocatalytic hydrogen evolution. For example, electrocatalysts based on the {Fe<sub>2</sub>S<sub>2</sub>} motif have been investigated experimentally<sup>32–43</sup> and theoretically<sup>44–46</sup> in the past decade. Catalytic and energetic efficiencies have seen ongoing advances stemming from the preparation of novel synthetic complexes or systems.

Proton-coupled electron transfer (PCET) is an important energy conversion process in chemical and biological systems; it proceeds by coupling protons and electrons together.<sup>47–65</sup> The coupled proton–electron transfer occurs by bypassing the unstable or unfavorable intermediate. Incorporating PCET into the electrocatalytic reactions could result in energetically and kinetically more efficient processes.<sup>66–73</sup> For electrochemical PCET, a great deal of effort has been given to the investigation of the redox behavior of aminophenol compounds, which were designed to mimic the oxidation of tyrosine in Photosystem II. In biological systems, histidine nearby acts as a proton acceptor when a tyrosyl radical is formed. Much progress on the fundamentals of PCET has been achieved by studying such aminophenol systems using electrochemical methods<sup>74–79</sup> and theoretical calculations.<sup>77–82</sup> From the aspect of hydrogen evolution, an electrocatalytic system based on a Ni–Ru molecular catalyst has been reported using Et<sub>3</sub>NH<sup>+</sup> as a proton source.<sup>83</sup> Density functional theory (DFT) calculations suggested that the PCET reaction occurred. In Co<sup>66,84</sup> and Ni<sup>21</sup> hangman porphyrin complexes, intramolecular proton transfer initiated by the hangman motif facilitated proton reduction at more positive potentials and led to faster proton transfer in comparison to that of the analogous non-hangman systems. Furthermore, a comprehensive theoretical study on a

Received: March 1, 2018

family of  $[\text{Ni}(\text{P}^{\text{R}}_2\text{N}^{\text{R}'}_2)_2]^{2+}$  complexes for  $\text{H}_2$  production has been performed.<sup>85–87</sup> The obtained Pourbaix diagrams and free-energy profiles provided valuable guidelines for proton management and ligand design in the PCET process. Recently, the formation of a Ni/S film during  $\text{H}_2$ -evolving electrocatalysis was suggested to be initiated by a PCET step.<sup>88,89</sup> Despite the fact that these pioneering works revealed some information on the kinetic and thermodynamic parameters governing the catalysis, more studies are necessary for a comprehensive understanding of the stepwise and concerted pathways in the electrocatalytic system.

In this work, the detailed mechanism of hydrogen evolution by  $[(\mu,\kappa^2\text{-bdt})(\mu\text{-PPh}_2)\text{Fe}_2(\text{CO})_5]^-$  in a wide range of acids is investigated. In contrast to the catalysis in trifluoromethanesulfonic acid (HOTf), trichloroacetic acid (TCA), and trifluoroacetic acid (TFA), which involves stepwise pathways, the catalytic reaction in the presence of anilinium acid occurs via a PCET pathway, which facilitates hydrogen evolution at the same potential as that of the HOTf catalysis. The instant effect regarding energy usage is that the overpotential is reduced by +0.4 V. In addition, the heterogeneous electron transfer rate is enhanced by up to 40 times according to the results of simulations of electrochemical data. The conjectured stepwise mechanism in the catalysis of anilinium acid by this catalyst is ruled out by the results of experiments, DFT calculations, and electroanalytic simulations. To the best of our knowledge, this is the first  $\text{Fe}_2\text{S}_2$  catalyst which exhibits a PCET-involved electrocatalysis. Substantial thermodynamic and kinetic benefits are observed in this effective catalytic system for hydrogen formation.

## RESULTS AND DISCUSSION

**Redox Chemistry of  $\text{I}^-$  and Electrocatalytic Hydrogen Evolution by  $\text{I}^-$ .** Cyclic voltammograms (CVs) of  $[(\mu,\kappa^2\text{-bdt})(\mu\text{-PPh}_2)\text{Fe}_2(\text{CO})_5]^-$  ( $\text{I}^-$ ; bdt = 1,2-benzenedithiolate) under acid-free conditions showed a reversible one-electron oxidation event at  $E_{1/2}^{\text{ox}} = -0.63$  V (vs  $\text{Fc}^+/\text{Fc}$ ; all potentials throughout the article are referenced against  $\text{Fc}^+/\text{Fc}$ ) in  $\text{CH}_2\text{Cl}_2$  solution (Figure 1). This process was diffusion-controlled, as indicated by the linear dependence of the peak current on the square root of the scan rate (Figure S2b). A reduction response was only displayed as the tail at the end of

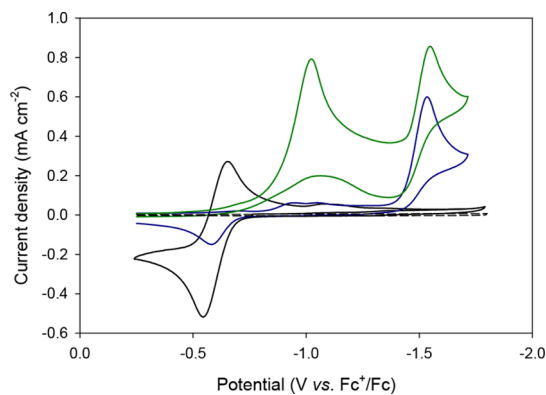


**Figure 1.** Cyclic voltammograms of  $\text{I}^-$  alone (black),  $1\mu\text{H}$  (from the reaction of  $\text{I}^-$  with 1 equiv of  $\text{HBARF}_{24}$ , blue), and  $1\mu\text{HSH}^+$  (from the reaction of  $\text{I}^-$  with 2 equiv of  $\text{HBARF}_{24}$ , green) in  $\text{CH}_2\text{Cl}_2$  solution (2.4 mM  $\text{I}^-$ ,  $v = 0.1$  V  $\text{s}^{-1}$ , 298 K). The background CV is shown as a dashed trace.

the accessible electrochemical window in  $\text{CH}_2\text{Cl}_2$  solution. The corresponding event was clearly observed at  $E_{1/2}^{\text{red}} = -2.37$  V in THF solution (Figure S2a). We reasonably estimated that the reduction of  $\text{I}^-$  in  $\text{CH}_2\text{Cl}_2$  solution would occur at an applied cathodic potential of  $-2.37$  V because  $\text{I}^-$  exhibited similar oxidation potentials in different media ( $-0.63$  and  $-0.62$  V in  $\text{CH}_2\text{Cl}_2$  and THF solutions, respectively).

In the presence of excess anilinium acid ( $[\text{PhNH}_3][\text{BARF}_{24}]$ ,  $\text{p}K_{\text{a}}^{\text{MeCN}} = 10.9$ ),<sup>90</sup> the CV of  $\text{I}^-$  exhibited two irreversible reduction steps at  $-1.16$  and  $-1.57$  V in  $\text{CH}_2\text{Cl}_2$  solution (Figure 2). The current density of the first reduction increased

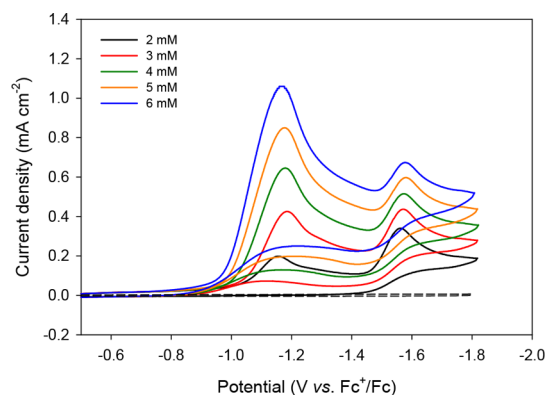


**Figure 2.** Cyclic voltammograms of  $\text{I}^-$  in  $\text{CH}_2\text{Cl}_2$  solution with increments of anilinium acid (1 mM  $\text{I}^-$ ,  $v = 0.1$  V  $\text{s}^{-1}$ , 0.1 M  $[\text{nBu}_4\text{N}][\text{BARF}_{24}]$ , 295 K) under  $\text{N}_2$ . All potentials were calibrated to the  $\text{Fc}^+/\text{Fc}$  pair as an internal standard. The background CV is shown as a dashed trace.

linearly with the square root of the acid concentration, whereas the current density of the second reduction did not, indicating that the first wave was the catalytic process. When the peak current of the catalytic wave was plotted against the square root of the scan rate, a linear dependence was obtained. This result suggests that the catalysis is diffusion-limited and is a homogeneous reaction.

When electrocatalysis was performed in the presence of excess TFA ( $\text{p}K_{\text{a}}^{\text{MeCN}} = 12.7$ )<sup>91</sup> or TCA ( $\text{p}K_{\text{a}}^{\text{MeCN}} = 10.6$ ),<sup>90</sup> one irreversible reduction event at  $-1.57$  V was recorded (Figure 3b and Figure S9, respectively). The current density increased linearly with the square root of the acid concentration, suggesting a catalytic process. Regarding the electrochemical behavior involving a strong acid, two reduction waves at  $-1.16$  and  $-1.57$  V were observed for  $\text{I}^-$  when the proton source was replaced by HOTf ( $\text{p}K_{\text{a}}^{\text{MeCN}} = 2.6$ ),<sup>90</sup> as shown in Figure 3a. The peak current of the redox event at  $-1.16$  V increased linearly with sequential increase of the added acids ( $i_{\text{cat}} \propto [\text{acid}]^{0.5}$ ), suggesting a catalytic response of hydrogen production. Among these acids, those of medium strength (TFA and TCA) exhibited one catalytic wave at  $-1.57$  V, whereas the wave was observed at  $-1.16$  V, accompanied by an additional noncatalytic process at  $-1.57$  V, for a stronger acid (HOTf). Anilinium acid displayed a different electrochemical behavior in comparison to TFA and TCA, even though they have similar  $\text{p}K_{\text{a}}$  values.

**Determination of the Intermediates and Dominant Reaction Pathways.** To elucidate the electrocatalytic hydrogen-evolution mechanism for various proton sources, we characterized intermediate species under acidic conditions and investigated possible catalytic routes. Reaction of  $\text{I}^-$  with

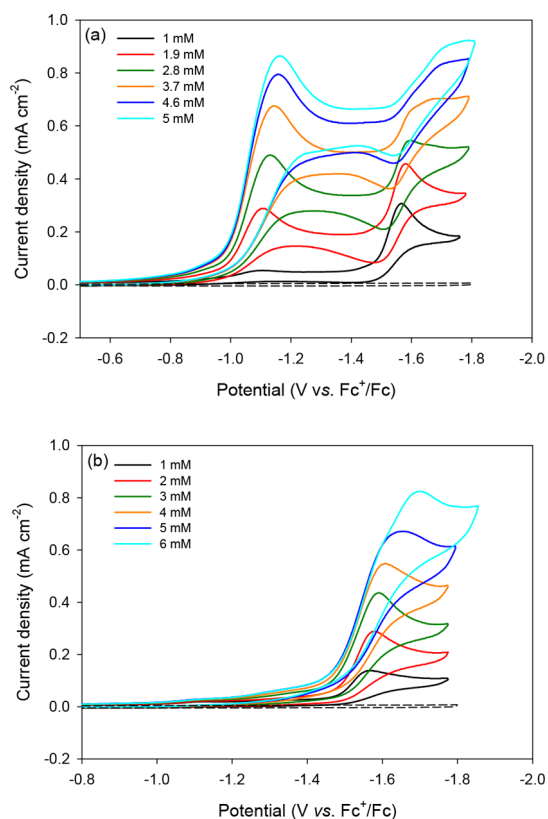
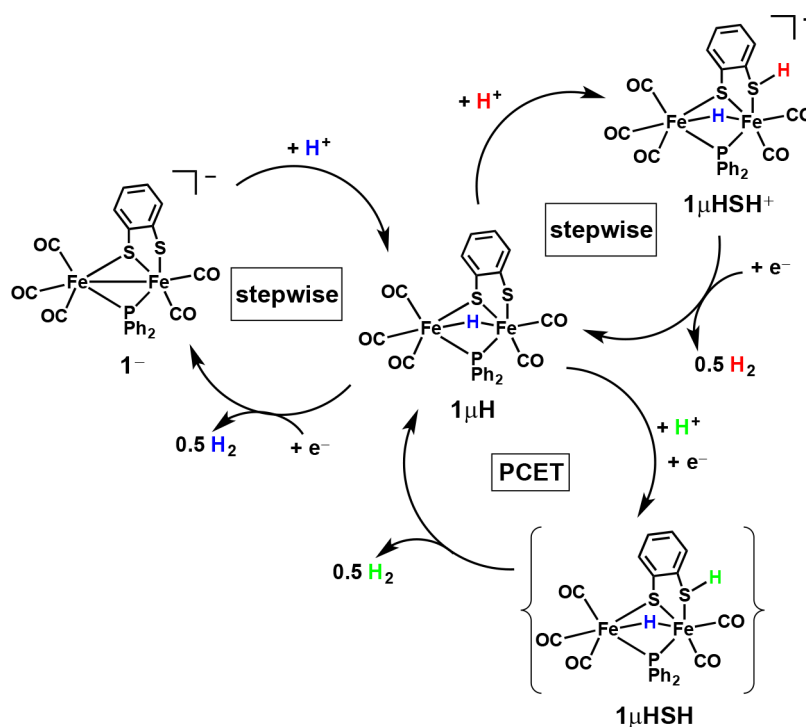


**Figure 3.** Cyclic voltammograms of  $\text{I}^-$  in  $\text{CH}_2\text{Cl}_2$  solution with increments of (a) HOTf and (b) TFA (1 mM  $\text{I}^-$ ,  $v = 0.1 \text{ V s}^{-1}$ , 0.1 M  $[\text{nBu}_4\text{N}][\text{BArF}_{24}]$ , 295 K) under  $\text{N}_2$ . All potentials were calibrated to the  $\text{Fc}^+/\text{Fc}$  pair as an internal standard. Background CVs are shown as dashed traces.

a stoichiometric amount of acid (e.g.,  $\text{HBarF}_{24}$  ( $\text{BArF}_{24}^- = \text{B}(3,5\text{-C}_6\text{H}_3(\text{CF}_3)_2)_4^-$ ), HOTf, TCA, anilinium acid, or TFA) afforded the monoprotonated species  $[(\mu, \kappa^2\text{-bdt})(\mu\text{-PPh}_2)(\mu\text{-H})\text{Fe}_2(\text{CO})_5]$  ( $\mathbf{1}\mu\text{H}$ ), as depicted in Scheme 1. Additional amounts of  $\text{HBarF}_{24}$  (or HOTf) led to the doubly protonated species  $[(\mu, \kappa^2\text{-bdtH})(\mu\text{-PPh}_2)(\mu\text{-H})\text{Fe}_2(\text{CO})_5]^+$  ( $\mathbf{1}\mu\text{HSH}^+$ ),<sup>92</sup> which cannot be obtained in the presence of excess TCA, TFA, and anilinium acid. The electrochemical behavior of both protonated species is displayed in Figure 1. Cathodic scans of  $\text{HBarF}_{24}$ -yielded  $\mathbf{1}\mu\text{HSH}^+$  revealed two irreversible waves at  $E_{\text{pc1}}(\mathbf{1}\mu\text{HSH}^+) = -1 \text{ V}$  and  $E_{\text{pc2}}(\mathbf{1}\mu\text{HSH}^+) = -1.57 \text{ V}$  and one irreversible wave at  $E_{\text{pc}}(\mathbf{1}\mu\text{H}) = -1.57 \text{ V}$  for  $\mathbf{1}\mu\text{H}$ . The first cathodic wave of the HOTf-yielded  $\mathbf{1}\mu\text{HSH}^+$  was recorded at  $-1.16 \text{ V}$ . The shift of 160 mV toward more negative potential was attributed to the influence of ion pairing, which plays a non-negligible role in electrochemical responses in solution.<sup>93</sup> The weak interaction between the  $[\text{OTf}]^-$  anion and the S proton of  $\mathbf{1}\mu\text{HSH}^+$  partially neutralized the positive charge, exerting a negative effect relative to  $\mathbf{1}\mu\text{HSH}^+$  in the noncoordinating  $[\text{BArF}_{24}]^-$  salt. Because these cathodic waves were approximately the same as those for the oxidation pair of  $\text{I}^-$  with respect to peak height after normalization, every irreversible reduction event corresponded to a one-electron charge transfer process when parameters for charge-transfer and mass-transfer phenomena in the redox reactions were treated in the same manner.

The chemical reduction of  $\mathbf{1}\mu\text{HSH}^+$  by 1 equiv of cobaltocene ( $\text{Cp}_2\text{Co}$ ,  $E_{1/2}^{\text{CH}_2\text{Cl}_2} = -1.33 \text{ V}$ )<sup>94</sup> yielded an IR profile that was changed only by a shift of approximately  $20 \text{ cm}^{-1}$  to lower energies (Figure S1a). This species was characterized to be the predecessor  $\mathbf{1}\mu\text{H}$ .<sup>92</sup> Regeneration of  $\text{I}^-$ , supported by the IR evidence, was achieved via the chemical

### Scheme 1. Schematic of Hydrogen Production by $\text{I}^-$ in the Presence of Acids<sup>a</sup>



<sup>a</sup>Hydrogen evolution occurs to  $\mathbf{1}\mu\text{HSH}^+$  and  $\mathbf{1}\mu\text{H}$  upon reduction.  $\mathbf{1}\mu\text{HSH}$  is a proposed transient species that has not been experimentally characterized.

reduction of  $\mathbf{1}\mu\mathbf{H}$  by decamethylcobaltocene ( $\text{Cp}^*\text{Co}$ ,  $E_{1/2}^{\text{CH}_2\text{Cl}_2} = -1.94 \text{ V}$ )<sup>94</sup> (Figure S1b). The results indicate that the first reduction in the CV of  $\mathbf{1}\mu\text{HSH}^+$  generated  $\mathbf{1}\mu\mathbf{H}$  and that the second wave originated from the reduction of  $\mathbf{1}\mu\mathbf{H}$ . The contents of the gaseous products from both redox events were analyzed by GC and were identified as  $\text{H}_2$  (Figure S1c). The reduction processes associated with the protonated species are summarized in Scheme 1.

The chemical reduction in the presence of acids was also investigated.  $\mathbf{1}\mu\mathbf{H}$  was the essential catalytic species because a negligible amount of hydrogen (<1% of the  $\text{H}_2$  amount from the catalyzed reaction) was detected for the reaction without the catalyst. Upon the reduction of  $\mathbf{1}\mu\mathbf{H}$  to  $\mathbf{1}\mu\mathbf{H}^-$ , hydrogen evolution could occur by either or both of the following mechanisms: a bimolecular reaction that involves loss of  $\text{H}^\bullet$  radical and a unimolecular reaction that involves the reaction of hydride with acid. In the former,  $\mathbf{1}\mu\mathbf{H}^-$  reacted to the other same species to yield  $\text{I}^-$  as well as  $\text{H}_2$ , and the as-generated  $\text{I}^-$  was readily reprotonated to  $\mathbf{1}\mu\mathbf{H}$ . The acid–base reaction via the unimolecular pathway generated the oxidized product  $\mathbf{1}$  and  $\text{H}_2$ . These two mechanisms are displayed in Scheme S2. Characterization of the reaction product enables us to determine the operating mechanism. When the solution containing 1 equiv of  $\mathbf{1}\mu\mathbf{H}$  and 3 equiv of TFA was subjected to 1 equiv of  $\text{Cp}^*\text{Co}$ , the solution species characterized by FTIR spectroscopy was  $\mathbf{1}\mu\mathbf{H}$  and acid, accompanied by the formation of hydrogen bubbles (84% yield, 0.42 equiv of  $\text{H}_2$ ). As the oxidized species  $\mathbf{1}$  and the disproportionation species  $\text{I}^-$  were not detected according to the in situ FTIR results, the possibilities of the heterolytic pathway and the disproportionation of  $\mathbf{1}$ , respectively, were ruled out. The results indicate that release of  $\text{H}_2$  from  $\mathbf{1}\mu\mathbf{H}^-$  is faster than the reaction between  $\mathbf{1}\mu\mathbf{H}^-$  and acid. The best explanation for the experimental results is that the bimolecular mechanism is operative for  $\text{H}_2$  evolution under the limited acid conditions. The same conclusion was drawn for the  $\mathbf{1}\mu\text{HSH}^+$  case.

We also used electroanalytical methods to confirm the bimolecular pathway being the operative catalytic mechanism: the passage of coulomb charge of the catalysis<sup>67,95</sup> and voltammetric responses as a function of  $\mathbf{1}\mu\mathbf{H}$ .<sup>96,97</sup> Under the electroreducing conditions,  $\text{I}^-$  is produced at the electrode surface with consumption of one electron per  $\text{Fe}_2$  if the bimolecular mechanism occurs. Constant-potential electrolysis of  $\mathbf{1}\mu\mathbf{H}$  at a potential of  $-1.7 \text{ V}$  resulted in the passage of 1.03 equiv of charge and the resultant species was characterized by FTIR spectroscopy to be  $\text{I}^-$ . The results suggested a net loss of  $\text{H}^\bullet$  radical from  $\mathbf{1}\mu\mathbf{H}^-$  for  $\text{H}_2$  evolution, following the reduction. The validity of this route was also evaluated by monitoring the peak current ratio with varied concentrations of  $\mathbf{1}\mu\mathbf{H}$ . The ratio  $i_{\text{pa}}'/i_{\text{pc}}$  reveals a quantitative measure of  $\text{I}^-$  formed ( $i_{\text{pa}}'$ ) relative to the concentration of  $\mathbf{1}\mu\mathbf{H}$  ( $i_{\text{pc}}$ ). If the bimolecular route is operative,  $i_{\text{pa}}'/i_{\text{pc}}$  reveals a linear dependence on the initial concentration of  $\mathbf{1}\mu\mathbf{H}$ ,  $[\mathbf{1}\mu\mathbf{H}]^0$ , in the absence of acid. As shown in Figure 4,  $i_{\text{pa}}'/i_{\text{pc}}$  increased with increasing  $[\mathbf{1}\mu\mathbf{H}]^0$  ranging from 0.6 to 3 mM at  $v = 50 \text{ V s}^{-1}$ , indicating that more  $\text{I}^-$  was generated when the higher  $[\mathbf{1}\mu\mathbf{H}]^0$  was employed. This lent additional support to the notion that  $\mathbf{1}\mu\mathbf{H}^-$  decays to  $\text{I}^-$  and  $\text{H}_2$  via the dominant homolytic pathway.

**Stepwise Mechanism involving HOTf, TCA, and TFA.** The irreversible reduction steps at  $-1.16$  and  $-1.57 \text{ V}$  in the electrochemical measurements of the  $\text{I}^-$ -HOTf system were assigned to the  $\mathbf{1}\mu\text{HSH}^{+/0}$  and  $\mathbf{1}\mu\text{H}^{0/-}$  events, respectively

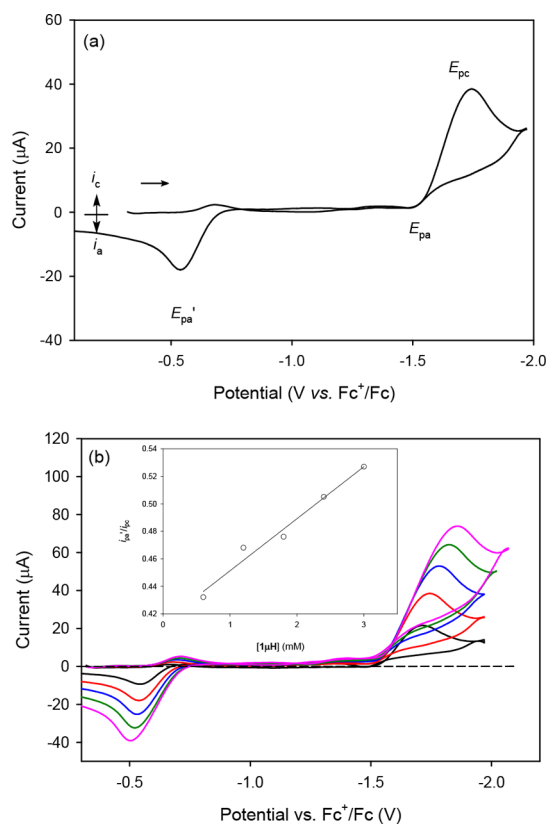
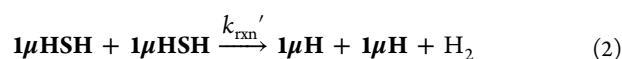


**Figure 4.** (a) Cyclic voltammogram of  $\mathbf{1}\mu\mathbf{H}$  (1.2 mM) at  $50 \text{ V s}^{-1}$  in  $\text{CH}_2\text{Cl}_2$  solution.  $i_{\text{pa}}'$  is defined as  $i_{\text{pa}}$  for the oxidation of  $\text{I}^-$ . (b) Cyclic voltammograms of  $\mathbf{1}\mu\mathbf{H}$  at  $50 \text{ V s}^{-1}$  at  $[\mathbf{1}\mu\mathbf{H}] = 0.6, 1.2, 1.8, 2.4, 3 \text{ mM}$ . The inset is the plot of  $i_{\text{pa}}'/i_{\text{pc}}$  vs initial concentration of  $\mathbf{1}\mu\mathbf{H}$  ( $R^2 = 0.9901$ ). The background CV is shown as a dashed trace.

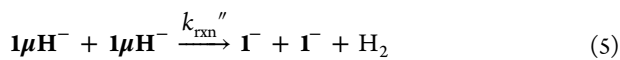
(Figure 3a). The proposed  $\text{H}_2$ -evolution pathways were constructed as follows:



One-electron reduction of the doubly protonated species  $\mathbf{1}\mu\text{HSH}^+$  proceeded with electron transfer rate  $k_s'$ . The subsequent bimolecular reaction converted  $\mathbf{1}\mu\text{HSH}$  into  $\mathbf{1}\mu\mathbf{H}$  with reaction rate  $k_{\text{rxn}}'$ . The catalytic cycle was completed by the regeneration of  $\mathbf{1}\mu\text{HSH}^+$  with proton transfer rate  $k_{\text{PT}}'$  and equilibrium constant  $K_{\text{eq}}'$  between  $\mathbf{1}\mu\mathbf{H}$  and  $\text{HOTf}$ . Here, the bimolecular (i.e., homolytic) pathway (eq 2) was chosen over the heterolytic pathway (i.e., the hydride-proton reaction) on the basis of our spectral and electrochemical results (vide supra). We employed digital simulation of the cyclic voltammograms on the basis of the proposed mechanism (Figure S7 and Table S7). The best-fit  $k_{\text{PT}}'$  and  $k_s'$  values were  $2.2 \times 10^5 \text{ s}^{-1} \text{ M}^{-1}$  and  $0.029 \text{ cm s}^{-1}$ , respectively.

Regarding TFA, TCA, and anilinium acid,  $\mathbf{1}\mu\mathbf{H}$  was the only product in the reaction of  $\text{I}^-$  with excess acids. The irreversible reduction at  $-1.57 \text{ V}$  was assigned to the  $\mathbf{1}\mu\text{H}^{0/-}$  process in the  $\text{I}^-$ -TFA and  $\text{I}^-$ -TCA systems. Similar to the catalysis of  $\mathbf{1}\mu\text{HSH}^+$ , the catalysis of  $\mathbf{1}\mu\mathbf{H}$  started with reduction, followed by hydrogen evolution via the bimolecular pathway and then

protonation to complete the cycle. The catalytic mechanism concerning  $\mathbf{1}\mu\mathbf{H}^{0/-}$  was described as follows:



The corresponding rate constant for each step was obtained from the least-squares fits to the experimental results, giving  $k_{\text{PT}}''$  and  $k_s''$  values of  $3495 \text{ s}^{-1} \text{ M}^{-1}$  and  $0.0162 \text{ cm}^3 \text{ s}^{-1}$ , respectively, for the TFA system. For the TCA system, the corresponding parameters were  $4198 \text{ s}^{-1} \text{ M}^{-1}$  and  $0.0219 \text{ cm}^3 \text{ s}^{-1}$ , respectively (Figures S8 and S10 and Tables S8 and S9).

In contrast to TFA and TCA, the different electrochemical behavior observed for anilinium acid suggested a new catalytic mechanism. Because the potentials for the catalytic responses of the  $\mathbf{1}\mu\mathbf{H}$ -[PhNH<sub>3</sub>][BArF<sub>24</sub>] system and  $\mathbf{1}\mu\mathbf{HSH}^+$  were very similar, we proposed an intermediate similar to the  $\mathbf{1}\mu\mathbf{HSH}$  species involved in the  $\mathbf{1}\mu\mathbf{H}$ -PhNH<sub>3</sub><sup>+</sup> system.

**Elucidation of the PCET Event.** Because both of the individual steps, i.e., proton transfer (PT) and electron transfer (ET), were not initially spontaneous in the reaction scheme of  $\mathbf{1}\mu\mathbf{H}$  in the  $\mathbf{1}\mu\mathbf{H}$ -PhNH<sub>3</sub><sup>+</sup> system, the catalytic process at  $-1.16 \text{ V}$  would most likely occur via a PCET step. We performed DFT calculations to obtain insights into the mechanistic routes and intermediates. Figure 5 gives a schematic of the states and

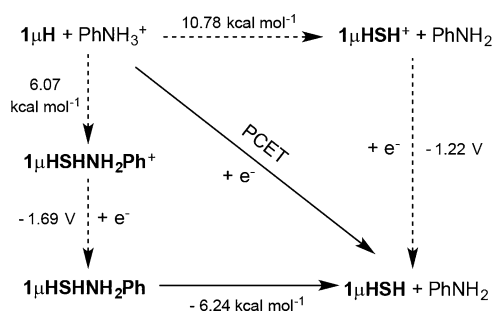


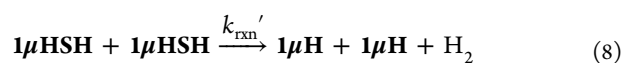
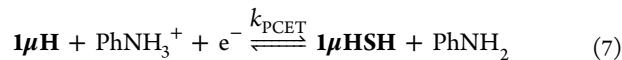
**Figure 5.** Theoretical thermochemistry of the  $\mathbf{1}\mu\mathbf{H}$ -PhNH<sub>3</sub><sup>+</sup> system in the catalysis. The dashed lines indicate the disfavored pathways. The calculated redox potentials are referenced to the Fc<sup>+</sup>/Fc pair.

charge transfer reactions in the  $\mathbf{1}\mu\mathbf{H}$ -PhNH<sub>3</sub><sup>+</sup> catalytic system. In the first stepwise mechanism, the initial PT was thermodynamically disfavored, with  $\Delta G_{\text{PT}}^\circ = 10.78 \text{ kcal mol}^{-1}$ . This result is consistent with the absence of  $\mathbf{1}\mu\mathbf{HSH}^+$  in solution. The subsequent ET occurred at the potential  $E^{\text{cal}}(\mathbf{1}\mu\mathbf{HSH}^{+/0}) = -1.22 \text{ V}$ . This step was observed in the HOTf catalysis by  $\mathbf{I}^-$ . This calculated redox potential value was considered to be reliable because any potential difference between the calculated and the experimental results was acceptable if it was smaller than  $400 \text{ mV}$ .<sup>98,99</sup>

Furthermore, we observed that, when  $\mathbf{1}\mu\mathbf{H}$  was in contact with excess anilinium acids (>20 equiv) at ambient temperature, the IR profile of  $\mathbf{1}\mu\mathbf{H}$  in solution shifted to higher energies by  $+8 \text{ cm}^{-1}$ , with the exhibition of three distinct  $\nu_{\text{CO}}$  bands at  $2088 \text{ (s)}$ ,  $2035 \text{ (vs)}$ , and  $1985 \text{ (m)}$   $\text{cm}^{-1}$  and one shoulder at  $2022 \text{ cm}^{-1}$  (Figure S16a). The moderate energy difference suggested that the electronic structure of  $\mathbf{1}\mu\mathbf{H}$  was partially perturbed by the surrounding PhNH<sub>3</sub><sup>+</sup> proton donors,

presumably due to the hydrogen-bond (H-bond) interactions. The <sup>1</sup>H NMR resonance for the H-bonded proton was observed at  $4.54 \text{ ppm}$  (Figures S17 and S18). The DFT-optimized structure of the H-bond-paired species  $\mathbf{1}\mu\mathbf{HSHNH}_2\text{Ph}^+$  revealed a short S⋯H contact of  $2.135 \text{ \AA}$  from one acidic proton of the anilinium cation toward the terminal thiolate of  $\mathbf{1}\mu\mathbf{H}$  (Figure S16c). This distance remained well within the sum of van der Waals radii. A similar H-bonding interaction between the S<sup>t</sup> of  $\mathbf{I}^-$  and *N,N*-dimethylanilinium acid was recently characterized at  $183 \text{ K}$ .<sup>100</sup> This observed H-bonding interaction supports the hypothesis that the S<sup>t</sup> site of  $\mathbf{1}\mu\mathbf{H}$  acts as the proton acceptor during catalysis. We then considered that the reduction accounting for the other mechanism was associated with the H-bonding interaction. The resulting H-bonded species  $\mathbf{1}\mu\mathbf{HSHNH}_2\text{Ph}^+$  was more stable than  $\mathbf{1}\mu\mathbf{H}$  by approximately  $5 \text{ kcal mol}^{-1}$  but was still unfavorable. A much smaller energy shift was anticipated for the transition from the  $\mathbf{1}\mu\mathbf{H}$  state to the  $\mathbf{1}\mu\mathbf{HSHNH}_2\text{Ph}^+$  state than for the conversion from  $\mathbf{1}\mu\mathbf{H}$  to  $\mathbf{1}\mu\mathbf{HSH}^+$  because the H-bonding interaction has less influence on the electronic structure of the complex in comparison to the full protonation. The calculated potential  $E^{\text{cal}}(\mathbf{1}\mu\mathbf{HSHNH}_2\text{Ph}^{+/0})$  was  $-1.69 \text{ V}$ . The resulting value showed a large deviation from the  $-1.16 \text{ V}$  obtained for the PCET process, even after a calibration of  $220 \text{ mV}$  was used to account for the theory–experiment difference for  $E(\mathbf{1}\mu\mathbf{HSH}^{+/0})$ . This result indicates that the driving force from the H-bonding interaction was not sufficiently strong to give rise to the positive potential shift that was compatible with the direct protonation. These results lent support to the suggestion that the PCET catalysis occurred in the  $\mathbf{1}\mu\mathbf{H}$ -PhNH<sub>3</sub><sup>+</sup> system.

**Kinetic Study of the PCET Event.** To disentangle the kinetic behavior of this PCET event ( $\mathbf{1}\mu\mathbf{HSH}^{\text{PCET}}$ ), we used a nonadiabatic Marcusian electron transfer formula for PCET step in the digital simulation. The mechanism was depicted as follows:



The cyclic voltammograms of  $\mathbf{1}\mu\mathbf{H}$  in the presence of stoichiometric amounts of PhNH<sub>3</sub><sup>+</sup> were obtained. The apparent heterogeneous rate constant  $k_{\text{PCET}}$  was optimized by fitting the cyclic voltammograms from different scan rates and various acid concentrations (Figure S11 and Table S10). The species  $\mathbf{1}\mu\mathbf{HSH}$  converts to  $\mathbf{1}\mu\mathbf{H}$  at a hydrogen production rate  $k_{\text{rxn}}'$  assumed to be  $1.92 \times 10^{10} \text{ s}^{-1} \text{ M}^{-1}$ , which is the value taken from the HOTf catalysis. The best-fitted results gave  $0.63 \text{ cm}^3 \text{ s}^{-1}$  for the  $k_{\text{PCET}}$  value.

It has also been pointed out that the potential shift between the catalytic and noncatalytic events may occur in stepwise reactions.<sup>76,84,101,102</sup> To examine the validity of the stepwise mechanism, we therefore decoupled the PCET event into hypothetical ETPT pathways as follows:

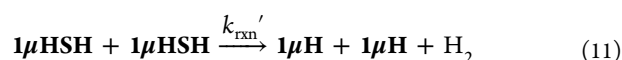


Table 1. Summary of Electrocatalytic Results

acid	$pK_a^{\text{MeCN}}$	$E_{\text{cat}}$ (V) <sup>a</sup>	overpotential (V) <sup>b</sup>	$k_{\text{PT}}$ (s <sup>-1</sup> M <sup>-1</sup> ) <sup>c</sup>	$k_s$ (cm s <sup>-1</sup> ) <sup>c</sup>	process
CF <sub>3</sub> SO <sub>3</sub> H	2.6	-1.16	+0.74	$2.2 \times 10^5$	0.0290	$1\mu\text{HSH}^{+/0}$
CCl <sub>3</sub> COOH	10.6	-1.57	+0.86	4198	0.0219	$1\mu\text{H}^{0/-}$
CF <sub>3</sub> COOH	12.7	-1.57	+0.82	3495	0.0162	$1\mu\text{H}^{0/-}$
[PhNH <sub>3</sub> ][BArF <sub>24</sub> ]	10.7	-1.16	+0.40	N/A	0.63	$1\mu\text{HSH}^{\text{PCET}}$

<sup>a</sup>All potentials are reported against the Fc<sup>+</sup>/Fc couple. <sup>b</sup>Overpotential =  $|E_{\text{H}^+} - E_{\text{cat}/2}|$ . The thermodynamic potential ( $E_{\text{H}^+}$ ) has been calibrated to a value for 10 mM of acid on the basis of eq 8 in *Inorg. Chem.* **2010**, *49*, 10338, except for HOTf, which is referenced to *Inorg. Chem.* **2006**, *45*, 9181. <sup>c</sup> $k_{\text{PT}}$  and  $k_s$  in the table are the general descriptions for individual PT and ET rates, respectively, in the different pathways.

Upon one-electron reduction, proton transfer simultaneously occurred at the rate  $k_{\text{PT}}''''$  to generate  $1\mu\text{HSH}$  as the ready-state species for H<sub>2</sub> evolution. The intramolecular pathway of H<sub>2</sub> evolution ( $1\mu\text{HSH} \rightarrow \text{I} + \text{H}_2$ ) was ruled out according to the DFT results (Scheme S1). In the simulations, the diffusion coefficients and  $k_{\text{rxn}}'$  values were assumed to be the same as those from the PCET pathways. The proton transfer rate  $k_{\text{PT}}''''$  was initially assumed to be the maximum diffusion rate  $k_{\text{Max-diff}}$  between  $1\mu\text{H}^-$  and PhNH<sub>3</sub><sup>+</sup>, which was estimated by the Debye–Smoluchowski method<sup>89,103</sup> (see the Supporting Information). The transfer coefficient  $\alpha$  and ET rate  $k_s''$  were separately tuned in curve fitting until the best fit on either the current amplitude or catalytic peak potential was achieved. Neither the experimental peak potential shift nor the current amplitude was reproduced in the simulations with the application of the  $k_{\text{Max-diff}}$  value of  $7.8 \times 10^9$  s<sup>-1</sup> M<sup>-1</sup> (Figure S13a–d). With an increase in the  $k_s''$  rate, the simulated peak potential anodically shifted to a potential boundary,  $\sim -1.35$  V. The results suggest the intermolecular PT to be a rate-limiting step in this hypothetical stepwise mechanism. In the previous estimation of  $k_{\text{Max-diff}}$ , the electrostatic interaction between the two charged species,  $1\mu\text{H}^-$  and PhNH<sub>3</sub><sup>+</sup>, was not considered. The maximum diffusion rate was corrected to  $k_{\text{Max-diff}}^{\text{Corr}}$  as the electrostatic interaction was included. Upon substituting a  $k_{\text{Max-diff}}^{\text{Corr}}$  value of  $2.15 \times 10^{15}$  s<sup>-1</sup> M<sup>-1</sup> for  $k_{\text{Max-diff}}$ , the best fit to the peak potential was able to be achieved by varying  $\alpha$  or  $k_s''$ . The resultant current amplitude, however, was largely deviated from the experimental data (Figure S13e–h). We could not obtain a satisfactory fit that fully reproduced the experimental current amplitude and catalytic peak potential when optimizing  $\alpha$  and  $k_s''$  in the simulation. It is said that the catalysis in the  $1\mu\text{H}$ -PhNH<sub>3</sub><sup>+</sup> system cannot be described as a stepwise ETPT reaction.

**Discussion of the PCET vs the Non-PCET Event.** In these studies, the catalytic performance of I<sup>-</sup> under various acids with  $pK_a$  values between 2.6 and 12.7 was investigated. Two observed catalytic processes were due to the  $1\mu\text{HSH}^{+/0}$  and  $1\mu\text{H}^{0/-}$  processes under the conditions of strong- and medium-strength acids, respectively. Notably, the employment of anilinium acid facilitated the PCET-involved catalytic process. To elucidate whether the  $pK_a$  value of an acid was decisive for the PCET reaction in our system, we compared the catalysis of TCA and anilinium acid, where both acids have similar  $pK_a$  values and afforded only  $1\mu\text{H}$  in solution. The electrocatalytic event occurred at -1.16 V for the I<sup>-</sup>-PhNH<sub>3</sub><sup>+</sup> system, more positive by 0.4 V than for the I<sup>-</sup>-TCA system. These results suggest that cationic anilinium acid rather than the  $pK_a$  of the proton sources was indispensable for the PCET reaction. For the overpotential, an energy savings of 0.4 V relative to the conventional stepwise processes (+0.4 V vs approximately +0.8 V, Table 1) was observed when the PCET process occurred, indicating that the PCET reaction offers a

substantial thermodynamic benefit for the catalysis. Importantly, the H/D kinetic isotope experiments showed similar catalytic current responses and identical reduction potentials under the same conditions (Table S11). The results suggest that the barrier in the intersection of the proton potential energy curves of the electrochemical PCET is small and that the overlap in the ground proton vibronic states is large. The PCET also affected the heterogeneous ET rate. The rate for the  $1\mu\text{HSH}^{\text{PCET}}$  process was on the order of 0.63 cm s<sup>-1</sup>, which is up to 40 times greater than the estimated rate of 0.016–0.029 cm s<sup>-1</sup> for the ordinary  $1\mu\text{H}^{0/-}$  and  $1\mu\text{HSH}^{+/0}$  processes. Overall, a decrease in the working potential and enhancement of the heterogeneous ET rate in the PCET event lead to an improvement in the catalytic performance relative to that of the stepwise processes (Table 1).

## CONCLUSION

In summary, the redox behavior of the Fe–S-containing catalyst I<sup>-</sup> was investigated and its electrocatalytic properties under various acidic conditions were characterized to proceed via two different hydrogen evolution processes that were ascribed to stepwise CCE (C, chemical reaction; E, one-electron reduction) and CE processes concerning the Fe-hydride-S-proton species and the Fe-hydride species, respectively. The use of anilinium acid as the proton source allowed the catalysis to occur via the PCET route. This pathway is associated with the concomitant PT from PhNH<sub>3</sub><sup>+</sup> to the S<sup>i</sup> of  $1\mu\text{H}$ , along with ET from the electrode surface to  $1\mu\text{H}$ . Here, we presented an example of the PCET catalysis for H<sub>2</sub> formation and showed that the careful management of Brønsted acid–base couples is capable of enhancing the catalytic performance. Further study of the electrocatalytic mechanisms associated with the proton-donating/-accepting ability is ongoing in our laboratory.

## EXPERIMENTAL SECTION

**General Methods.** All reactions were carried out by using standard Schlenk and vacuum-line techniques under an atmosphere of purified nitrogen. All commercially available chemicals from Aldrich were of ACS grade and were used without further purification. Solvents were of HPLC grade and were purified as follows. Hexane, diethyl ether, and tetrahydrofuran (THF) were distilled from sodium/benzophenone under N<sub>2</sub>. Dichloromethane was distilled from CaH<sub>2</sub> under N<sub>2</sub>. Acetonitrile (MeCN) was distilled first over CaH<sub>2</sub> and then from P<sub>2</sub>O<sub>5</sub> under N<sub>2</sub>. Deuterated solvents obtained from Merck were distilled over 4 Å molecular sieves under N<sub>2</sub> prior to use.

Infrared spectra were recorded on a PerkinElmer Spectrum One instrument using a 0.05 mm CaF<sub>2</sub> cell. <sup>1</sup>H, <sup>13</sup>C{<sup>1</sup>H}, and <sup>31</sup>P{<sup>1</sup>H} NMR spectra were recorded on a Bruker AV-500 or DRX-500 spectrometer operating at 500, 125.7, and 202.49 MHz, respectively. <sup>1</sup>H-DOSY NMR spectra were recorded on a 600 MHz Varian VNMRs spectrometer at 298 K. Mass spectral analyses were done on a Waters LCT Premier XE instrument at the Mass Spectrometry Center of the Institute of Chemistry, Academia Sinica. Elemental analyses were performed on an Elementar vario EL III elemental analyzer. Analysis

of H<sub>2</sub> gas from controlled-potential electrolysis and chemical reduction reactions was performed on an Agilent 7890 gas chromatograph equipped with a thermal conductivity detector (TCD) and fitted with a Restek ShinCarbon ST column (100/120 mesh, 2 m, 1/16 in. o.d., 1.0 mm i.d.). The column temperature was kept at 80 °C, and the injection and detector were both at 200 °C. The gas flow was 15 mL min<sup>-1</sup>. Nitrogen was used as the carrier gas.

**Molecular Structure Determination.** The X-ray single-crystal crystallographic data collection for [TBA][1] (CCDC 976229) was carried out at 150 K on a Bruker SMART APEX CCD four-circle diffractometer with graphite-monochromated Mo K $\alpha$  radiation ( $\lambda$  = 0.71073 Å) outfitted with a low-temperature, nitrogen-stream aperture. The structures were solved using direct methods, in conjunction with standard difference Fourier techniques, and refined by full-matrix least-squares procedures. A summary of the crystallographic data for complex 1<sup>-</sup> is shown in Table S1. An empirical absorption correction (multiscan) was applied to the diffraction data for all structures. All non-hydrogen atoms were refined anisotropically, and all hydrogen atoms were placed in geometrically calculated positions by the riding model. All software used for diffraction data processing and crystal structure solution and refinement are contained in the SHELXTL97 program suites.<sup>104</sup> In [TBA][( $\mu,\kappa^2$ -bdt)( $\mu$ -PPh<sub>2</sub>)Fe<sub>2</sub>(CO)<sub>5</sub>]-THF, two of the butyl carbon atoms in the <sup>n</sup>Bu<sub>4</sub>N<sup>+</sup> cation (C34, C35) are disordered.

**Electrochemistry.** Electrochemical measurements were recorded on a CH Instruments 630C electrochemical potentiostat using a gastight three-electrode cell under N<sub>2</sub> at 298 K unless otherwise stated. A vitreous carbon electrode (1 or 3 mm in diameter) and a platinum wire were used as working and auxiliary electrodes, respectively. The reference electrode was a nonaqueous Ag<sup>+</sup>/Ag electrode (0.01 M AgNO<sub>3</sub>/0.1 M [<sup>n</sup>Bu<sub>4</sub>N][BArF<sub>24</sub>]<sup>105</sup> BArF<sub>24</sub><sup>-</sup> = B(3,5-C<sub>6</sub>H<sub>3</sub>(CF<sub>3</sub>)<sub>2</sub>)<sub>4</sub><sup>-</sup>). The reference electrode was in a separate compartment with a Vycor glass tip. The working and counter electrodes were in the same compartment when the CVs were collected. The working electrode was polished after each scan. All potentials were measured in CH<sub>2</sub>Cl<sub>2</sub> or THF solution containing 0.1 M [<sup>n</sup>Bu<sub>4</sub>N][BArF<sub>24</sub>]. The potentials are reported against the ferrocenium/ferrocene (Fc<sup>+</sup>/Fc) couple. All measurements were performed with *iR* compensation. The simulation of the cyclic voltammetry was performed using the DigiElch 7.FD program on the background-corrected data.

Controlled-potential electrolysis (CPE) was performed in a three-electrode cell under N<sub>2</sub> at 298 or 273 K. The working and counter electrodes were graphite rods (6.15 mm in diameter) and were separated in two compartments when the CPE experiments were performed. The compartment containing the counter electrode had a 10 mm diameter fine-porosity glass frit. The CPEs were performed at -1.1 and -1.6 V (vs Fc<sup>+</sup>/Fc) for hydrogen production from **1** $\mu$ HSH<sup>+</sup> and **1** $\mu$ H, respectively. The potential for the PCET reaction involving **1** $\mu$ H in the presence of anilinium acid was performed at -1.1 V (vs Fc<sup>+</sup>/Fc). Regarding the Faradaic efficiency (FE) and turnover number (TON), three runs were conducted at each potential for 1 h at 298 K. The FTIR results indicated that the catalyst remained stable during the CPE conducted at 273 K. The reported FEs and TONs were the average values over three sets of the data. Following CPE, 250  $\mu$ L of headspace gas was removed from the working electrode compartment with a gastight syringe (Hamilton SampleLock) and was analyzed on an Agilent 7890 gas chromatograph. The amount of hydrogen was determined in comparison to a standard calibration curve from known amounts of hydrogen. From the determined amount of hydrogen generated, TON and FE were calculated according to the following equations, respectively: TON =  $n/n_{\text{cat}}$ ; FE (%) =  $2nF/Q_{\text{cat}} \times 100\%$ , where  $n$  is the number of moles of hydrogen produced,  $n_{\text{cat}}$  is the number of moles of the catalyst,  $F$  is the Faraday constant, and  $Q_{\text{cat}}$  is the total amount of charge passed in the CPE.

Prolonged CPE concerning anilinium acid was performed at 298 K for 12 h, in which the catalytic current revealed a significant decrease after  $t > 7000$  s (see the Supporting Information). The major solution species was **1** $\mu$ H according to the FTIR results. Most of the proton source was consumed, which is possibly responsible for the current decay over time. The other plausible explanation is the formation of

the daughter species [( $\mu$ -bdt)Fe<sub>2</sub>(CO)<sub>5</sub>(PPh<sub>2</sub>H)] and [( $\mu,\mu,\kappa_2$ -bdt)<sub>4</sub>( $\mu$ -PPh<sub>2</sub>)<sub>4</sub>Fe<sub>8</sub>(CO)<sub>18</sub>]. **1** $\mu$ H was reported to slowly convert to [( $\mu$ -bdt)Fe<sub>2</sub>(CO)<sub>5</sub>(PPh<sub>2</sub>H)] in solution.<sup>92</sup> It was reported that [( $\mu,\mu,\kappa_2$ -bdt)<sub>4</sub>( $\mu$ -PPh<sub>2</sub>)<sub>4</sub>Fe<sub>8</sub>(CO)<sub>18</sub>] was generated from oxidation of 1.<sup>106</sup>

**Synthesis.** *Synthesis of [TBA][( $\mu,\kappa^2$ -bdt)( $\mu$ -PPh<sub>2</sub>)Fe<sub>2</sub>(CO)<sub>5</sub>]* ([TBA]-[1]). The preparation procedures are similar to those published previously.<sup>92</sup> To a red THF solution (30 mL) of [( $\mu$ -bdt)-Fe<sub>2</sub>(CO)<sub>6</sub>]<sup>107</sup> (500 mg, 1.19 mmol) was added a 0.5 M solution of KPPH<sub>2</sub> (2.4 mL, 1.2 mmol) in THF. The brown solution was stirred overnight and dried in vacuo. The green-brown solution was mixed with 50 mL of acetone, followed by addition of 330 mg (1.19 mmol) of tetrabutylammonium chloride (TBACl). The reaction mixture was stirred at room temperature for 3 h, and the solvent was removed in vacuo. The residue was dissolved in 20 mL of CH<sub>2</sub>Cl<sub>2</sub>, and the solution was filtered through Celite to remove insoluble salt. The product was precipitated upon addition of hexane. The green-brown solid was washed three times with 20 mL of ether and 30 mL of hexane and then dried under vacuum. The yield was 761 mg (78%). Crystals of [TBA][( $\mu,\kappa^2$ -bdt)( $\mu$ -PPh<sub>2</sub>)Fe<sub>2</sub>(CO)<sub>5</sub>]-THF suitable for X-ray crystallographic analysis were grown from a THF/hexane solution at -20 °C. IR (THF, cm<sup>-1</sup>):  $\nu_{\text{CO}}$  2005 m, 1961 vs, 1936 m, 1916 s, 1896 m. <sup>1</sup>H NMR (500 MHz, *d*-THF, 295 K): 0.97 (t, 12H, CH<sub>3</sub> of TBA<sup>+</sup>), 1.36 (m, 8H, CH<sub>2</sub> of TBA<sup>+</sup>), 1.60 (m, 8H, CH<sub>2</sub> of TBA<sup>+</sup>), 3.15 (m, 8H, NCH<sub>2</sub> of TBA<sup>+</sup>), 6.63 (t, 1H, <sup>3</sup>J<sub>HH</sub> = 7.0 Hz, S<sub>2</sub>C<sub>6</sub>H<sub>4</sub>), 6.72 (t, 1H, <sup>3</sup>J<sub>HH</sub> = 7.0 Hz, S<sub>2</sub>C<sub>6</sub>H<sub>4</sub>), 7.11 (m, 3H, P(C<sub>6</sub>H<sub>5</sub>)<sub>2</sub>), 7.21 (m, 3H, P(C<sub>6</sub>H<sub>5</sub>)<sub>2</sub>), 7.42 (d, 1H, <sup>3</sup>J<sub>HH</sub> = 8 Hz, S<sub>2</sub>C<sub>6</sub>H<sub>4</sub>), 7.54 (m, 3H, S<sub>2</sub>C<sub>6</sub>H<sub>4</sub>, P(C<sub>6</sub>H<sub>5</sub>)<sub>2</sub>), 7.72 (m, 2H, P(C<sub>6</sub>H<sub>5</sub>)<sub>2</sub>) ppm. <sup>13</sup>C{<sup>1</sup>H} NMR (125.7 MHz, *d*-THF, 298 K): 12.95 (s, 4C, CH<sub>3</sub> of TBA<sup>+</sup>), 19.66 (s, 4C, CH<sub>2</sub> of TBA<sup>+</sup>), 23.68 (s, 4C, CH<sub>2</sub> of TBA<sup>+</sup>), 58.49 (s, 4C, NCH<sub>2</sub> of TBA<sup>+</sup>), 117.86 (s, 1C, S<sub>2</sub>C<sub>6</sub>H<sub>4</sub>), 122.97 (s, 1C, S<sub>2</sub>C<sub>6</sub>H<sub>4</sub>), 126.61 (d, 2C, J<sub>PC</sub> = 9.3 Hz, P(C<sub>6</sub>H<sub>5</sub>)<sub>2</sub>), 127.16 (d, 2C, J<sub>PC</sub> = 9.7 Hz, P(C<sub>6</sub>H<sub>5</sub>)<sub>2</sub>), 127.41 (s, 1C, P(C<sub>6</sub>H<sub>5</sub>)<sub>2</sub>), 127.91 (s, 1C, P(C<sub>6</sub>H<sub>5</sub>)<sub>2</sub>), 128.76 (s, 1C, S<sub>2</sub>C<sub>6</sub>H<sub>4</sub>), 129.33 (s, 1C, S<sub>2</sub>C<sub>6</sub>H<sub>4</sub>), 133.68 (m, 4C, P(C<sub>6</sub>H<sub>5</sub>)<sub>2</sub>), 139.59 (d, 1C, J = 21.3 Hz, *ipso*-S<sub>2</sub>C<sub>6</sub>H<sub>4</sub>), 141.25 (d, 1C, J<sub>PC</sub> = 34.7 Hz, *ipso*-P(C<sub>6</sub>H<sub>5</sub>)<sub>2</sub>), 144.09 (d, 1C, J<sub>PC</sub> = 26.3 Hz, *ipso*-P(C<sub>6</sub>H<sub>5</sub>)<sub>2</sub>), 160.17 (s, 1C, *ipso*-S<sub>2</sub>C<sub>6</sub>H<sub>4</sub>), 216.67 (d, 3C, J<sub>PC</sub> = 3.4 Hz, CO), 218.81 (d, 1C, J<sub>PC</sub> = 10.2 Hz, CO), 220.98 (d, 1C, J<sub>PC</sub> = 18.9 Hz, CO) ppm. <sup>31</sup>P{<sup>1</sup>H} NMR (202.48 MHz, *d*-THF, 296 K): 144.7 (s) ppm. ESI-MS:  $m/z$  576.9 {M}<sup>+</sup>, 548.9 {M - CO}<sup>+</sup>, 520.9 {M - 2CO}<sup>+</sup>, 492.9 {M - 3CO}<sup>+</sup>, 464.9 {M - 4CO}<sup>+</sup>, 436.9 {M - 5CO}<sup>+</sup>. Anal. Calcd for C<sub>39</sub>H<sub>50</sub>Fe<sub>2</sub>NO<sub>5</sub>PS<sub>2</sub>: N, 1.71; C, 57.15; H, 6.15. Found: N, 1.92, C, 57.04; H, 6.12.

*Reaction of [TBA][( $\mu,\kappa^2$ -bdt)( $\mu$ -PPh<sub>2</sub>)Fe<sub>2</sub>(CO)<sub>5</sub>] with [PhNH<sub>3</sub>]-[BArF<sub>24</sub>].* To a CH<sub>2</sub>Cl<sub>2</sub> solution (10 mL) of [TBA][( $\mu,\kappa^2$ -bdt)( $\mu$ -PPh<sub>2</sub>)Fe<sub>2</sub>(CO)<sub>5</sub>] (100 mg, 0.122 mmol) was added a CH<sub>2</sub>Cl<sub>2</sub> solution (10 mL) of [PhNH<sub>3</sub>][BArF<sub>24</sub>]<sup>108</sup> (143 mg, 0.15 mmol). The IR profile was changed from 2005 m, 1961 vs, 1936, 1916, and 1896 m cm<sup>-1</sup> to 2080 s, 2030 vs, 2013 s and 1983 m cm<sup>-1</sup>, as monitored by FTIR spectroscopy. The profile was shifted to higher energy upon addition of an additional 29 equiv of [PhNH<sub>3</sub>][BArF<sub>24</sub>] in CH<sub>2</sub>Cl<sub>2</sub> solution. IR (CH<sub>2</sub>Cl<sub>2</sub>, cm<sup>-1</sup>):  $\nu_{\text{CO}}$  2088 s, 2035 vs, 2022 sh, 1985 m cm<sup>-1</sup>.

*Reaction of [TBA][( $\mu,\kappa^2$ -bdt)( $\mu$ -PPh<sub>2</sub>)Fe<sub>2</sub>(CO)<sub>5</sub>] with CF<sub>3</sub>COOH.* A CH<sub>2</sub>Cl<sub>2</sub> solution (5 mL) of [TBA][( $\mu,\kappa^2$ -bdt)( $\mu$ -PPh<sub>2</sub>)Fe<sub>2</sub>(CO)<sub>5</sub>] (50 mg, 0.061 mmol) was treated with CF<sub>3</sub>COOH (10  $\mu$ L, 0.13 mmol). The IR profile was changed from 2005 m, 1961 vs, 1936, 1916, and 1896 m cm<sup>-1</sup> to 2081 s, 2030 vs, 2013 s, and 1983 m cm<sup>-1</sup>, as monitored by FTIR spectroscopy. The profile was shifted to higher energy upon addition of a further 28 equiv of CF<sub>3</sub>COOH in CH<sub>2</sub>Cl<sub>2</sub> solution. IR (CH<sub>2</sub>Cl<sub>2</sub>, cm<sup>-1</sup>):  $\nu_{\text{CO}}$  2083 s, 2034 vs, 2022 sh, 1985 m cm<sup>-1</sup>.

*Reaction of [TBA][( $\mu,\kappa^2$ -bdt)( $\mu$ -PPh<sub>2</sub>)Fe<sub>2</sub>(CO)<sub>5</sub>] with CCl<sub>3</sub>COOH.* A CH<sub>2</sub>Cl<sub>2</sub> solution (5 mL) of [TBA][( $\mu,\kappa^2$ -bdt)( $\mu$ -PPh<sub>2</sub>)Fe<sub>2</sub>(CO)<sub>5</sub>] (50 mg, 0.061 mmol) was treated with CCl<sub>3</sub>COOH (13 mg, 0.08 mmol). The IR profile was changed from 2005 m, 1961 vs, 1936, 1916, and 1896 m cm<sup>-1</sup> to 2081 s, 2031 vs, 2013 s, and 1984 m cm<sup>-1</sup>, as monitored by FTIR spectroscopy. The profile was unchanged upon addition of a further 29 equiv of CCl<sub>3</sub>COOH in CH<sub>2</sub>Cl<sub>2</sub> solution.

*Reduction of [( $\mu,\kappa^2$ -bdtH)( $\mu$ -PPh<sub>2</sub>)( $\mu$ -H)Fe<sub>2</sub>(CO)<sub>5</sub>][OTf] ([1 $\mu$ HSH]-[OTf]) by Cobaltocene (Cp<sub>2</sub>Co).* Chemical reduction of **1** $\mu$ HSH<sup>+</sup><sup>92</sup>

was conducted in  $\text{CH}_2\text{Cl}_2$  solution at 299 K. To a  $\text{CH}_2\text{Cl}_2$  solution (7 mL) of  $\mathbf{1}\mu\text{HSH}^+$  (100 mg, 0.137 mmol) was added a  $\text{CH}_2\text{Cl}_2$  solution (5 mL) of cobaltocene (26 mg, 0.137 mmol). An instant color change to green was observed. The original IR bands were shifted from 2101 s, 2059 vs, 2045 s, and 2019  $\text{m cm}^{-1}$  to lower energies at 2081 s, 2030 vs, 2013 s, and 1984  $\text{m cm}^{-1}$ , confirming the formation of  $\mathbf{1}\mu\text{H}$ . The content of gaseous products in the headspace of the Schlenk flask was analyzed by GC to be  $\text{H}_2$ .

**Reduction of  $[(\mu,\kappa^2\text{-bdt})(\mu\text{-PPh}_2)(\mu\text{-H})\text{Fe}_2(\text{CO})_5]$  ( $\mathbf{1}\mu\text{H}$ ) by Decamethylcobaltocene ( $\text{Cp}^*\text{Co}$ ).** Chemical reduction of  $\mathbf{1}\mu\text{H}$  was conducted in  $\text{CH}_2\text{Cl}_2$  solution at 299 K. To a  $\text{CH}_2\text{Cl}_2$  solution (7 mL) of  $\mathbf{1}\mu\text{H}$  (80 mg, 0.138 mmol) was added a  $\text{CH}_2\text{Cl}_2$  solution (5 mL) of  $\text{Cp}^*\text{Co}$  (68 mg, 0.207 mmol). The solution was stirred for 1 h and measured by FTIR spectroscopy. The IR bands shifted from 2081 s, 2030 vs, 2013 s, and 1984  $\text{m cm}^{-1}$  to lower energies at 2004 m, 1961 vs, 1933 m, 1917 s, and 1896  $\text{m cm}^{-1}$ , confirming the formation of  $\mathbf{1}^-$ . The content of gaseous products in the headspace of the Schlenk flask was analyzed by GC to be  $\text{H}_2$ .

## ■ ASSOCIATED CONTENT

### 📄 Supporting Information

The Supporting Information is available free of charge on the ACS Publications website at DOI: 10.1021/acs.inorgchem.8b00543.

Results of spectroscopy, electrochemistry, gas chromatography, and computational chemistry (PDF)

### Accession Codes

CCDC 976229 contains the supplementary crystallographic data for this paper. These data can be obtained free of charge via [www.ccdc.cam.ac.uk/data\\_request/cif](http://www.ccdc.cam.ac.uk/data_request/cif), or by emailing [data\\_request@ccdc.cam.ac.uk](mailto:data_request@ccdc.cam.ac.uk), or by contacting The Cambridge Crystallographic Data Centre, 12 Union Road, Cambridge CB2 1EZ, UK; fax: +44 1223 336033.

## ■ AUTHOR INFORMATION

### Corresponding Authors

\*E-mail for Y.-C.L.: [yuchiao@gate.sinica.edu.tw](mailto:yuchiao@gate.sinica.edu.tw).

\*E-mail for M.-H.C.: [mhchiang@chem.sinica.edu.tw](mailto:mhchiang@chem.sinica.edu.tw).

### ORCID

Ming-Hsi Chiang: 0000-0002-7632-9369

### Notes

The authors declare no competing financial interest.

## ■ ACKNOWLEDGMENTS

This work was supported by the Ministry of Science and Technology of Taiwan and Academia Sinica. Professor Marcetta Y. Darensbourg (TAMU) and Professor Wen-Feng Liaw (NTHU) are acknowledged for helpful discussions. The authors are grateful to Professor Thomas B. Rauchfuss (UIUC) for his insightful suggestions. The authors also thank Dr. Mei-Chun Tseng (AS), Ms. Mei-Ying Chung (AS), and Ms. Li-Ching Shen (NCTU) for assistance with MS, EA, and  $^1\text{H}$ -DOSY NMR measurements, respectively. We are grateful to the High Performance Computing Service of Academia Sinica Computer Center (ASCC) and the National Center for High-performance Computing (NCHC) for computer time and facilities. The authors also thank the reviewers for helpful suggestions on mechanistic elucidation.

## ■ REFERENCES

- (1) *Hydrogen as a Fuel: Learning from Nature*; Cammack, R.; Frey, M., Robson, R., Eds.; Taylor & Francis: New York, 2001; p 267.
- (2) Lubitz, W.; Tumas, W. Hydrogen: An overview. *Chem. Rev.* **2007**, *107*, 3900–3903.
- (3) Cortright, R. D.; Davda, R. R.; Dumesic, J. A. Hydrogen from catalytic reforming of biomass-derived hydrocarbons in liquid water. *Nature* **2002**, *418*, 964–967.
- (4) Rostrup-Nielsen, J. R.; Sehested, J.; Nørskov, J. K. Hydrogen and synthesis gas by steam- and  $\text{CO}_2$  reforming. *Adv. Catal.* **2002**, *47*, 65–139.
- (5) Carroll, M. E.; Barton, B. E.; Rauchfuss, T. B.; Carroll, P. J. Synthetic models for the active site of the [FeFe]-hydrogenase: Catalytic proton reduction and the structure of the doubly protonated intermediate. *J. Am. Chem. Soc.* **2012**, *134*, 18843–18852.
- (6) Borg, S. J.; Behrsing, T.; Best, S. P.; Razavet, M.; Liu, X.; Pickett, C. J. Electron Transfer at a Dithiolate-Bridged Diiron Assembly: Electrocatalytic Hydrogen Evolution. *J. Am. Chem. Soc.* **2004**, *126*, 16988–16999.
- (7) Hsieh, C. H.; Ding, S. D.; Erdem, O. F.; Crouthers, D. J.; Liu, T. B.; McCrory, C. C. L.; Lubitz, W.; Popescu, C. V.; Reibenspies, J. H.; Hall, M. B.; Darensbourg, M. Y. Redox active iron nitrosyl units in proton reduction electrocatalysis. *Nat. Commun.* **2014**, *5*, 3684.
- (8) Gloaguen, F.; Rauchfuss, T. B. Small molecule mimics of hydrogenases: Hydrides and redox. *Chem. Soc. Rev.* **2009**, *38*, 100–108.
- (9) Tard, C.; Pickett, C. J. Structural and functional analogues of the active sites of the [Fe]-, [NiFe]-, and [FeFe]-hydrogenases. *Chem. Rev.* **2009**, *109*, 2245–2274.
- (10) Capon, J. F.; Gloaguen, F.; Schollhammer, P.; Talarmin, J. Catalysis of the electrochemical  $\text{H}_2$  evolution by di-iron sub-site models. *Coord. Chem. Rev.* **2005**, *249*, 1664–1676.
- (11) Samuel, A. P. S.; Co, D. T.; Stern, C. L.; Wasielewski, M. R. Ultrafast Photodriven Intramolecular Electron Transfer from a Zinc Porphyrin to a Readily Reduced Diiron Hydrogenase Model Complex. *J. Am. Chem. Soc.* **2010**, *132*, 8813–8815.
- (12) Ghosh, P.; Quiroz, M.; Wang, N.; Bhuvanesh, N.; Darensbourg, M. Y. Complexes of  $\text{MN}_2\text{S}_2$  center dot  $\text{Fe}(\eta^5\text{-C}_5\text{R}_5)(\text{CO})$  as platform for exploring cooperative heterobimetallic effects in HER electrocatalysis. *Dalton Trans.* **2017**, *46*, 5617–5624.
- (13) Harshan, A. K.; Solis, B. H.; Winkler, J. R.; Gray, H. B.; Hammes-Schiffer, S. Computational Study of Fluorinated Diglyoxime-Iron Complexes: Tuning the Electrocatalytic Pathways for Hydrogen Evolution. *Inorg. Chem.* **2016**, *55*, 2934–2940.
- (14) Seo, J.; Manes, T. A.; Rose, M. J. Structural and functional synthetic model of mono-iron hydrogenase featuring an anthracene scaffold. *Nat. Chem.* **2017**, *9*, 552–557.
- (15) Nguyen, A. D.; Rail, M. D.; Shanmugam, M.; Fettinger, J. C.; Berben, L. A. Electrocatalytic Hydrogen Evolution from Water by a Series of Iron Carbonyl Clusters. *Inorg. Chem.* **2013**, *52*, 12847–12854.
- (16) Han, Z. J.; McNamara, W. R.; Eum, M. S.; Holland, P. L.; Eisenberg, R. A nickel thiolate catalyst for the long-lived photocatalytic production of hydrogen in a noble-metal-free system. *Angew. Chem., Int. Ed.* **2012**, *51*, 1667–1670.
- (17) Le Goff, A.; Artero, V.; Jousset, B.; Tran, P. D.; Guillet, N.; Métayé, R.; Fihri, A.; Palacin, S.; Fontecave, M. From hydrogenases to noble metal-free catalytic nanomaterials for  $\text{H}_2$  production and uptake. *Science* **2009**, *326*, 1384–1387.
- (18) Stewart, M. P.; Ho, M.-H.; Wiese, S.; Lindstrom, M. L.; Thogerson, C. E.; Raugei, S.; Bullock, R. M.; Helm, M. L. High Catalytic Rates for Hydrogen Production Using Nickel Electrocatalysts with Seven-Membered Cyclic Diphosphine Ligands Containing One Pendant Amine. *J. Am. Chem. Soc.* **2013**, *135*, 6033–6046.
- (19) Reback, M. L.; Buchko, G. W.; Kier, B. L.; Ginovska-Pangovska, B.; Xiong, Y.; Lense, S.; Hou, J.; Roberts, J. A. S.; Sorensen, C. M.; Raugei, S.; Squier, T. C.; Shaw, W. J. Enzyme Design from the Bottom Up: An Active Nickel Electrocatalyst with a Structured Peptide Outer Coordination Sphere. *Chem. - Eur. J.* **2014**, *20*, 1510–1514.
- (20) Helm, M. L.; Stewart, M. P.; Bullock, R. M.; DuBois, M. R.; DuBois, D. L. A synthetic nickel electrocatalyst with a turnover

frequency above  $100,000\text{ s}^{-1}$  for  $\text{H}_2$  production. *Science* **2011**, *333*, 863–866.

(21) Bediako, D. K.; Solis, B. H.; Dogutan, D. K.; Roubelakis, M. M.; Maher, A. G.; Lee, C. H.; Chambers, M. B.; Hammes-Schiffer, S.; Nocera, D. G. Role of pendant proton relays and proton-coupled electron transfer on the hydrogen evolution reaction by nickel hangman porphyrins. *Proc. Natl. Acad. Sci. U. S. A.* **2014**, *111*, 15001–15006.

(22) Brazzolotto, D.; Gennari, M.; Queyriaux, N.; Simmons, T. R.; Pecaut, J.; Demeshko, S.; Meyer, F.; Orio, M.; Artero, V.; Duboc, C. Nickel-centred proton reduction catalysis in a model of NiFe hydrogenase. *Nat. Chem.* **2016**, *8*, 1054–1060.

(23) McCrory, C. C. L.; Uyeda, C.; Peters, J. C. Electrocatalytic hydrogen evolution in acidic water with molecular cobalt tetraazamacrocycles. *J. Am. Chem. Soc.* **2012**, *134*, 3164–3170.

(24) Dempsey, J. L.; Brunschwig, B. S.; Winkler, J. R.; Gray, H. B. Hydrogen evolution catalyzed by cobaloximes. *Acc. Chem. Res.* **2009**, *42*, 1995–2004.

(25) Chen, L.; Wang, M.; Han, K.; Zhang, P.; Gloaguen, F.; Sun, L. A super-efficient cobalt catalyst for electrochemical hydrogen production from neutral water with 80 mV overpotential. *Energy Environ. Sci.* **2014**, *7*, 329–334.

(26) Singh, W. M.; Mirmohades, M.; Jane, R. T.; White, T. A.; Hammarström, L.; Thapper, A.; Lomoth, R.; Ott, S. Voltammetric and spectroscopic characterization of early intermediates in the Co(II)-polypyridyl-catalyzed reduction of water. *Chem. Commun.* **2013**, *49*, 8638–8640.

(27) Letko, C. S.; Panetier, J. A.; Head-Gordon, M.; Tilley, T. D. Mechanism of the Electrocatalytic Reduction of Protons with Diaryldithiolene Cobalt Complexes. *J. Am. Chem. Soc.* **2014**, *136*, 9364–9376.

(28) Lee, C. H.; Dogutan, D. K.; Nocera, D. G. Hydrogen Generation by Hangman Metalloporphyrins. *J. Am. Chem. Soc.* **2011**, *133*, 8775–8777.

(29) van der Meer, M.; Glais, E.; Siewert, I.; Sarkar, B. Electrocatalytic Dihydrogen Production with a Robust Mesoionic Pyridylcarbene Cobalt Catalyst. *Angew. Chem., Int. Ed.* **2015**, *54*, 13792–13795.

(30) Karunadasa, H. I.; Chang, C. J.; Long, J. R. A molecular molybdenum-oxo catalyst for generating hydrogen from water. *Nature* **2010**, *464*, 1329–1333.

(31) Appel, A. M.; DuBois, D. L.; DuBois, M. R. Molybdenum-sulfur dimers as electrocatalysts for the production of hydrogen at low overpotentials. *J. Am. Chem. Soc.* **2005**, *127*, 12717–12726.

(32) Camara, J. M.; Rauchfuss, T. B. Combining acid-base, redox and substrate binding functionalities to give a complete model for the [FeFe]-hydrogenase. *Nat. Chem.* **2012**, *4*, 26–30.

(33) Felton, G. A. N.; Vannucci, A. K.; Chen, J. Z.; Lockett, L. T.; Okumura, N.; Petro, B. J.; Zakai, U. I.; Evans, D. H.; Glass, R. S.; Lichtenberger, D. L. Hydrogen generation from weak acids: Electrochemical and computational studies of a diiron hydrogenase mimic. *J. Am. Chem. Soc.* **2007**, *129*, 12521–12530.

(34) Chouffai, D.; Capon, J.-F.; De Gioia, L.; Pétilion, F. Y.; Schollhammer, P.; Talarmin, J.; Zampella, G. A Diferrous Dithiolate as a Model of the Elusive  $\text{H}_{\text{ox}}^{\text{inact}}$  State of the [FeFe] Hydrogenases: An Electrochemical and Theoretical Dissection of Its Redox Chemistry. *Inorg. Chem.* **2015**, *54*, 299–311.

(35) Gloaguen, F. Electrochemistry of Simple Organometallic Models of Iron-Iron Hydrogenases in Organic Solvent and Water. *Inorg. Chem.* **2016**, *55*, 390–398.

(36) Gilbert-Wilson, R.; Siebel, J. F.; Adamska-Venkatesh, A.; Pham, C. C.; Reijerse, E.; Wang, H. X.; Cramer, S. P.; Lubitz, W.; Rauchfuss, T. B. Spectroscopic Investigations of [FeFe] Hydrogenase Maturated with  $[\text{Fe}_2(\text{adt})(\text{CN})_2(\text{CO})_4]^{2-}$ . *J. Am. Chem. Soc.* **2015**, *137*, 8998–9005.

(37) Crouthers, D. J.; Denny, J. A.; Bethel, R. D.; Munoz, D. G.; Darensbourg, M. Y. Conformational Mobility and Pendant Base Effects on Electrochemistry of Synthetic Analogues of the FeFe-Hydrogenase Active Site. *Organometallics* **2014**, *33*, 4747–4755.

(38) Jablonskytė, A.; Wright, J. A.; Fairhurst, S. A.; Peck, J. N. T.; Ibrahim, S. K.; Oganessian, V. S.; Pickett, C. J. Paramagnetic Bridging Hydrides of Relevance to Catalytic Hydrogen Evolution at Metallo-sulfur Centers. *J. Am. Chem. Soc.* **2011**, *133*, 18606–18609.

(39) Zheng, D. H.; Wang, N.; Wang, M.; Ding, S. D.; Ma, C. B.; Darensbourg, M. Y.; Hall, M. B.; Sun, L. C. Intramolecular Iron-Mediated C-H Bond Heterolysis with an Assist of Pendant Base in a [FeFe]-Hydrogenase Model. *J. Am. Chem. Soc.* **2014**, *136*, 16817–16823.

(40) Wright, R. J.; Zhang, W.; Yang, X. Z.; Fasulo, M.; Tilley, T. D. Isolation, observation, and computational modeling of proposed intermediates in catalytic proton reductions with the hydrogenase mimic  $\text{Fe}_2(\text{CO})_6\text{S}_2\text{C}_6\text{H}_4$ . *Dalton Trans.* **2012**, *41*, 73–82.

(41) Cheah, M. H.; Tard, C.; Borg, S. J.; Liu, X. M.; Ibrahim, S. K.; Pickett, C. J.; Best, S. P. Modeling Fe-Fe hydrogenase: evidence for bridging carbonyl and distal iron coordination vacancy in an electrocatalytically competent proton reduction by an iron thiolate assembly that operates through Fe(0)-Fe(II) levels. *J. Am. Chem. Soc.* **2007**, *129*, 11085–11092.

(42) Carroll, M. E.; Barton, B. E.; Gray, D. L.; Mack, A. E.; Rauchfuss, T. B. Active-Site Models for the Nickel-Iron Hydrogenases: Effects of Ligands on Reactivity and Catalytic Properties. *Inorg. Chem.* **2011**, *50*, 9554–9563.

(43) Singleton, M. L.; Crouthers, D. J.; Duttweiler, R. P.; Reibenspies, J. H.; Darensbourg, M. Y. Sulfonated Diiron Complexes as Water-Soluble Models of the [FeFe]-Hydrogenase Enzyme Active Site. *Inorg. Chem.* **2011**, *50*, 5015–5026.

(44) Ryde, U.; Greco, C.; De Gioia, L. Quantum Refinement of [FeFe] Hydrogenase Indicates a Dithiomethylamine Ligand. *J. Am. Chem. Soc.* **2010**, *132*, 4512–4513.

(45) Greco, C.; Bruschi, M.; Fantucci, P.; Ryde, U.; De Gioia, L. Mechanistic and Physiological Implications of the Interplay among Iron-Sulfur Clusters in [FeFe]-Hydrogenases. A QM/MM Perspective. *J. Am. Chem. Soc.* **2011**, *133*, 18742–18749.

(46) Siegbahn, P. E. M.; Tye, J. W.; Hall, M. B. Computational studies of [NiFe] and [FeFe] hydrogenases. *Chem. Rev.* **2007**, *107*, 4414–4435.

(47) Hammes-Schiffer, S. Theory of Proton-Coupled Electron Transfer in Energy Conversion Processes. *Acc. Chem. Res.* **2009**, *42*, 1881–1889.

(48) Reece, S. Y.; Nocera, D. G. Proton-Coupled Electron Transfer in Biology: Results from Synergistic Studies in Natural and Model Systems. *Annu. Rev. Biochem.* **2009**, *78*, 673–699.

(49) Warren, J. J.; Tronic, T. A.; Mayer, J. M. Thermochemistry of proton-coupled electron transfer reagents and its implications. *Chem. Rev.* **2010**, *110*, 6961–7001.

(50) Weinberg, D. R.; Gagliardi, C. J.; Hull, J. F.; Murphy, C. F.; Kent, C. A.; Westlake, B. C.; Paul, A.; Ess, D. H.; McCafferty, D. G.; Meyer, T. J. Proton-coupled electron transfer. *Chem. Rev.* **2012**, *112*, 4016–4093.

(51) Migliore, A.; Polizzi, N. F.; Therien, M. J.; Beratan, D. N. Biochemistry and Theory of Proton-Coupled Electron Transfer. *Chem. Rev.* **2014**, *114*, 3381–3465.

(52) Cattaneo, M.; Ryken, S. A.; Mayer, J. M. Outer-Sphere  $2\text{e}^-/2\text{H}^+$  Transfer Reactions of Ruthenium(II)-Amine and Ruthenium(IV)-Amido Complexes. *Angew. Chem., Int. Ed.* **2017**, *56*, 3675–3678.

(53) Bergner, M.; Dechert, S.; Demeshko, S.; Kupper, C.; Mayer, J. M.; Meyer, F. Model of the MitoNEET [2Fe-2S] Cluster Shows Proton Coupled Electron Transfer. *J. Am. Chem. Soc.* **2017**, *139*, 701–707.

(54) Saouma, C. T.; Morris, W. D.; Darcy, J. W.; Mayer, J. M. Protonation and Proton-Coupled Electron Transfer at S-Ligated [4Fe-4S] Clusters. *Chem. - Eur. J.* **2015**, *21*, 9256–9260.

(55) Song, N.; Gagliardi, C. J.; Binstead, R. A.; Zhang, M. T.; Thorp, H.; Meyer, T. J. Role of Proton-Coupled Electron Transfer in the Redox Interconversion between Benzoquinone and Hydroquinone. *J. Am. Chem. Soc.* **2012**, *134*, 18538–18541.

- (56) Gagliardi, C. J.; Vannucci, A. K.; Concepcion, J. J.; Chen, Z. F.; Meyer, T. J. The role of proton coupled electron transfer in water oxidation. *Energy Environ. Sci.* **2012**, *5*, 7704–7717.
- (57) Chen, Z. F.; Vannucci, A. K.; Concepcion, J. J.; Jurss, J. W.; Meyer, T. J. Proton-coupled electron transfer at modified electrodes by multiple pathways. *Proc. Natl. Acad. Sci. U. S. A.* **2011**, *108*, E1461–E1469.
- (58) Soetbeer, J.; Dongare, P.; Hammarström, L. Marcus-type driving force correlations reveal the mechanism of proton-coupled electron transfer for phenols and [Ru(bpy)<sub>3</sub>]<sup>3+</sup> in water at low pH. *Chem. Sci.* **2016**, *7*, 4607–4612.
- (59) Dongare, P.; Maji, S.; Hammarström, L. Direct Evidence of a Tryptophan Analogue Radical Formed in a Concerted Electron-Proton Transfer Reaction in Water. *J. Am. Chem. Soc.* **2016**, *138*, 2194–2199.
- (60) Megiatto, J. D., Jr.; Méndez-Hernández, D. D.; Tejada-Ferrari, M. E.; Teillout, A. L.; Llansola-Portolés, M. J.; Kodis, G.; Poluektov, O. G.; Rajh, T.; Mujica, V.; Groy, T. L.; Gust, D.; Moore, T. A.; Moore, A. L. A bioinspired redox relay that mimics radical interactions of the Tyr-His pairs of photosystem II. *Nat. Chem.* **2014**, *6*, 423–428.
- (61) Zhang, M. T.; Nilsson, J.; Hammarström, L. Bimolecular proton-coupled electron transfer from tryptophan with water as the proton acceptor. *Energy Environ. Sci.* **2012**, *5*, 7732–7736.
- (62) Moore, G. F.; Hamburger, M.; Gervald, M.; Poluektov, O. G.; Rajh, T.; Gust, D.; Moore, T. A.; Moore, A. L. A bioinspired construct that mimics the proton coupled electron transfer between P680<sup>+</sup> and the Tyr<sub>z</sub>-His190 pair of photosystem II. *J. Am. Chem. Soc.* **2008**, *130*, 10466–10467.
- (63) Ravensbergen, J.; Brown, C. L.; Moore, G. F.; Frese, R. N.; van Grondelle, R.; Gust, D.; Moore, T. A.; Moore, A. L.; Kennis, J. T. M. Kinetic isotope effect of proton-coupled electron transfer in a hydrogen bonded phenol-pyrrolidino[60]fullerene. *Photochem. Photobiol. Sci.* **2015**, *14*, 2147–2150.
- (64) Wenger, O. S. Proton-coupled electron transfer with photoexcited ruthenium(II), rhenium(I), and iridium(III) complexes. *Coord. Chem. Rev.* **2015**, *282-283*, 150–158.
- (65) Cukier, R. I.; Nocera, D. G. Proton-coupled electron transfer. *Annu. Rev. Phys. Chem.* **1998**, *49*, 337–369.
- (66) Solis, B. H.; Hammes-Schiffer, S. Proton-Coupled Electron Transfer in Molecular Electrocatalysis: Theoretical Methods and Design Principles. *Inorg. Chem.* **2014**, *53*, 6427–6443.
- (67) Elgrishi, N.; McCarthy, B. D.; Rountree, E. S.; Dempsey, J. L. Reaction Pathways of Hydrogen-Evolving Electrocatalysts: Electrochemical and Spectroscopic Studies of Proton-Coupled Electron Transfer Processes. *ACS Catal.* **2016**, *6*, 3644–3659.
- (68) Costentin, C. Electrochemical approach to the mechanistic study of proton-coupled electron transfer. *Chem. Rev.* **2008**, *108*, 2145–2179.
- (69) Savéant, J. M. Electrochemical approach to proton-coupled electron transfers: recent advances. *Energy Environ. Sci.* **2012**, *5*, 7718–7731.
- (70) Costentin, C.; Robert, M.; Savéant, J. M. Concerted Proton-Electron Transfers: Electrochemical and Related Approaches. *Acc. Chem. Res.* **2010**, *43*, 1019–1029.
- (71) Coutard, N.; Kaefter, N.; Artero, V. Molecular engineered nanomaterials for catalytic hydrogen evolution and oxidation. *Chem. Commun.* **2016**, *52*, 13728–13748.
- (72) Ertem, M. Z.; Gagliardi, L.; Cramer, C. J. Quantum chemical characterization of the mechanism of an iron-based water oxidation catalyst. *Chem. Sci.* **2012**, *3*, 1293–1299.
- (73) Cukier, R. I. Proton-coupled electron transfer reactions: Evaluation of rate constants. *J. Phys. Chem.* **1996**, *100*, 15428–15443.
- (74) Costentin, C.; Robert, M.; Savéant, J. M.; Tard, C. Inserting a Hydrogen-Bond Relay between Proton Exchanging Sites in Proton-Coupled Electron Transfers. *Angew. Chem., Int. Ed.* **2010**, *49*, 3803–3806.
- (75) Costentin, C.; Robert, M.; Savéant, J. M. Reorganization energies and pre-exponential factors in the one-electron electrochemical and homogeneous oxidation of phenols coupled with an intramolecular amine-driven proton transfer. *Phys. Chem. Chem. Phys.* **2010**, *12*, 13061–13069.
- (76) Costentin, C.; Louault, C.; Robert, M.; Savéant, J. M. The electrochemical approach to concerted proton-electron transfers in the oxidation of phenols in water. *Proc. Natl. Acad. Sci. U. S. A.* **2009**, *106*, 18143–18148.
- (77) Costentin, C.; Robert, M.; Savéant, J. M. Electrochemical and homogeneous proton-coupled electron transfers: Concerted pathways in the one-electron oxidation of a phenol coupled with an intramolecular amine-driven proton transfer. *J. Am. Chem. Soc.* **2006**, *128*, 4552–4553.
- (78) Costentin, C.; Robert, M.; Savéant, J. M. Electrochemical concerted proton and electron transfers. Potential-dependent rate constant, reorganization factors, proton tunneling and isotope effects. *J. Electroanal. Chem.* **2006**, *588*, 197–206.
- (79) Costentin, C.; Robert, M.; Savéant, J. M. Adiabatic and non-adiabatic concerted proton-electron transfers. Temperature effects in the oxidation of intramolecularly hydrogen-bonded phenols. *J. Am. Chem. Soc.* **2007**, *129*, 9953–9963.
- (80) Auer, B.; Fernandez, L. E.; Hammes-Schiffer, S. Theoretical Analysis of Proton Relays in Electrochemical Proton-Coupled Electron Transfer. *J. Am. Chem. Soc.* **2011**, *133*, 8282–8292.
- (81) Markle, T. F.; Tenderholt, A. L.; Mayer, J. M. Probing Quantum and Dynamic Effects in Concerted Proton-Electron Transfer Reactions of Phenol-Base Compounds. *J. Phys. Chem. B* **2012**, *116*, 571–584.
- (82) Ghosh, S.; Soudackov, A. V.; Hammes-Schiffer, S. Electrochemical Electron Transfer and Proton-Coupled Electron Transfer: Effects of Double Layer and Ionic Environment on Solvent Reorganization Energies. *J. Chem. Theory Comput.* **2016**, *12*, 2917–2925.
- (83) Canaguier, S.; Fourmond, V.; Perotto, C. U.; Fize, J.; Pécaut, J.; Fontecave, M.; Field, M. J.; Artero, V. Catalytic hydrogen production by a Ni-Ru mimic of NiFe hydrogenases involves a proton-coupled electron transfer step. *Chem. Commun.* **2013**, *49*, 5004–5006.
- (84) Roubelakis, M. M.; Bediako, D. K.; Dogutan, D. K.; Nocera, D. G. Proton-coupled electron transfer kinetics for the hydrogen evolution reaction of hangman porphyrins. *Energy Environ. Sci.* **2012**, *5*, 7737–7740.
- (85) Small, Y. A.; DuBois, D. L.; Fujita, E.; Muckerman, J. T. Proton management as a design principle for hydrogenase-inspired catalysts. *Energy Environ. Sci.* **2011**, *4*, 3008–3020.
- (86) Horvath, S.; Fernandez, L. E.; Soudackov, A. V.; Hammes-Schiffer, S. Insights into proton-coupled electron transfer mechanisms of electrocatalytic H<sub>2</sub> oxidation and production. *Proc. Natl. Acad. Sci. U. S. A.* **2012**, *109*, 15663–15668.
- (87) Appel, A. M.; Pool, D. H.; O'Hagan, M.; Shaw, W. J.; Yang, J. Y.; DuBois, M. R.; DuBois, D. L.; Bullock, R. M. [Ni-(P<sup>Ph</sup><sub>2</sub>N<sup>BN</sup><sub>2</sub>)<sub>2</sub>(CH<sub>3</sub>CN)]<sup>2+</sup> as an Electrocatalyst for H<sub>2</sub> Production: Dependence on Add Strength and Isomer Distribution. *ACS Catal.* **2011**, *1*, 777–785.
- (88) Martin, D. J.; McCarthy, B. D.; Donley, C. L.; Dempsey, J. L. Electrochemical hydrogenation of a homogeneous nickel complex to form a surface adsorbed hydrogen-evolving species. *Chem. Commun.* **2015**, *51*, 5290–5293.
- (89) McCarthy, B. D.; Donley, C. L.; Dempsey, J. L. Electrode initiated proton-coupled electron transfer to promote degradation of a nickel(II) coordination complex. *Chem. Sci.* **2015**, *6*, 2827–2834.
- (90) Felton, G. A. N.; Glass, R. S.; Lichtenberger, D. L.; Evans, D. H. Iron-only hydrogenase mimics. Thermodynamic aspects of the use of electrochemistry to evaluate catalytic efficiency for hydrogen generation. *Inorg. Chem.* **2006**, *45*, 9181–9184.
- (91) Barton, B. E.; Rauchfuss, T. B. Hydride-Containing Models for the Active Site of the Nickel-Iron Hydrogenases. *J. Am. Chem. Soc.* **2010**, *132*, 14877–14885.
- (92) Liu, Y.-C.; Chu, K.-T.; Jhang, R.-L.; Lee, G.-H.; Chiang, M.-H. [FeFe] hydrogenase active site modeling: a key intermediate bearing a thiolate proton and Fe hydride. *Chem. Commun.* **2013**, *49*, 4743–4745.

- (93) Geiger, W. E.; Barrière, F. Organometallic Electrochemistry Based on Electrolytes Containing Weakly-Coordinating Fluoroarylborate Anions. *Acc. Chem. Res.* **2010**, *43*, 1030–1039.
- (94) Connelly, N. G.; Geiger, W. E. Chemical redox agents for organometallic chemistry. *Chem. Rev.* **1996**, *96*, 877–910.
- (95) Wiedner, E. S.; Roberts, J. A. S.; Dougherty, W. G.; Kassel, W. S.; DuBois, D. L.; Bullock, R. M. Synthesis and Electrochemical Studies of Cobalt(III) Monohydride Complexes Containing Pendant Amines. *Inorg. Chem.* **2013**, *52*, 9975–9988.
- (96) Koelle, U.; Paul, S. Electrochemical Reduction of Protonated Cyclopentadienylcobalt Phosphine Complexes. *Inorg. Chem.* **1986**, *25*, 2689–2694.
- (97) Olmstead, M. L.; Hamilton, R. G.; Nicholson, R. S. Theory of Cyclic Voltammetry for a Dimerization Reaction Initiated Electrochemically. *Anal. Chem.* **1969**, *41*, 260–267.
- (98) Hughes, T. F.; Friesner, R. A. Systematic Investigation of the Catalytic Cycle of a Single Site Ruthenium Oxygen Evolving Complex Using Density Functional Theory. *J. Phys. Chem. B* **2011**, *115*, 9280–9289.
- (99) Keith, J. A.; Carter, E. A. Theoretical Insights into Pyridinium-Based Photoelectrocatalytic Reduction of CO<sub>2</sub>. *J. Am. Chem. Soc.* **2012**, *134*, 7580–7583.
- (100) Chu, K.-T.; Liu, Y.-C.; Huang, Y.-L.; Hsu, C.-H.; Lee, G.-H.; Chiang, M.-H. A Reversible Proton Relay Process Mediated by Hydrogen-Bonding Interactions in [FeFe] Hydrogenase Modeling. *Chem. - Eur. J.* **2015**, *21*, 10978–10982.
- (101) Nicholson, R. S.; Shain, I. Theory of stationary electrode polarography. single scan and cyclic methods applied to reversible, irreversible, and kinetic systems. *Anal. Chem.* **1964**, *36*, 706–723.
- (102) Rountree, E. S.; Dempsey, J. L. Potential-Dependent Electrocatalytic Pathways: Controlling Reactivity with pK<sub>a</sub> for Mechanistic Investigation of a Nickel-Based Hydrogen Evolution Catalyst. *J. Am. Chem. Soc.* **2015**, *137*, 13371–13380.
- (103) Hatano, Y.; Katsumura, Y.; Mozumder, A.: *Charged particle and photon interactions with matter: recent advances, applications, and interfaces*; CRC Press: Boca Raton, FL, 2011.
- (104) *SHELXTL. ver. 6.10 ed.*; Bruker Analytical X-Ray Systems; Madison, WI, 2000.
- (105) Tellers, D. M.; Yung, C. M.; Arndtsen, B. A.; Adamson, D. R.; Bergman, R. G. Electronic and medium effects on the rate of arene C-H bond activation by cationic Ir(III) complexes. *J. Am. Chem. Soc.* **2002**, *124*, 1400–1410.
- (106) Chu, K. T.; Liu, Y. C.; Huang, Y. L.; Lee, G. H.; Tseng, M. C.; Chiang, M. H. Redox Communication within Multinuclear Iron-Sulfur Complexes Related to Electronic Interplay in the Active Site of FeFe Hydrogenase. *Chem. - Eur. J.* **2015**, *21*, 6852–6861.
- (107) Cabeza, J. A.; Martínez-García, M. A.; Riera, V.; Ardura, D.; García-Granda, S. Binuclear iron(I), ruthenium(I), and osmium(I) hexacarbonyl complexes containing a bridging benzene-1,2-dithiolate ligand. Synthesis, X-ray structures, protonation reactions, and EHMO calculations. *Organometallics* **1998**, *17*, 1471–1477.
- (108) Papish, E. T.; Rix, F. C.; Spetseris, N.; Norton, J. R.; Williams, R. D. Protonation of CpW(CO)<sub>2</sub>(PMe<sub>3</sub>)H: Is the metal or the hydride the kinetic site? *J. Am. Chem. Soc.* **2000**, *122*, 12235–12242.